energies

MDPI

Article

Effect of the Backward Facing Step on a Transverse Jet in Supersonic Crossflow

Jincheng Zhang *, Zhenguo Wang, Mingbo Sun, Hongbo Wang, Chaoyang Liu and Jiangfei Yu

Science and Technology on Scramjet Laboratory, National University of Defense Technology, Changsha 410073, China; zgwang@nudt.edu.cn (Z.W.); sunmingbo@nudt.edu.cn (M.S.); whbwatch@nudt.edu.cn (H.W.); liuchaoyang08@nudt.edu.cn (C.L.); jiangfeiyu@nudt.edu.cn (J.Y.)

* Correspondence: zhangjincheng_512@163.com

Received: 28 June 2020; Accepted: 11 August 2020; Published: 12 August 2020

Abstract: A transverse jet in the supersonic crossflow is one of the most promising injection schemes in scramjet, where the control or enhancement of jet mixing is a critical issue. In this paper, the effect of the backward facing step on the characteristics of jet mixing was investigated by three-dimensional large eddy simulation (LES). The simulation in the flat plate configuration (step height of 0) was performed as the baseline case to verify the computation framework. The distribution of the velocity and pressure obtained by the LES agreed well with the experiment, which shows the reliability of the LES code. Then, two steps with a height of 1.0D and 1.58D (D is the injector diameter) were numerically compared to the non-step baseline case. The comparison of the three cases illustrates the effect of the large-scale recirculation region on the variable distribution, and shock and vortex structures in the flow field. In the windward region, the shear layers become thicker, and the convection velocity of the shear vortexes reduces. In the leeward region, the wake vortices almost disappear while the counterrotating vortex pairs (CVPs) expand in the spanwise direction. In the area upstream of the jet, the separation bubble works with the upstream large-scale recirculation zone to entrain the jet into the upstream near-wall zone. At last, a comparison of the overall mixing performance of the three cases revealed that the penetration depth and mixing efficiency increased with the step height increasing.

Keywords: scramjet; LES; transverse jet; backward facing step; mixing enhancement

1. Introduction

Scramjet is one of the most popular engine technologies that achieve hypersonic flight, and its further development requires optimization of the overall performance. The mixing process, which is substantially affected by the geometric configurations and injection strategy, is a key factor in determining the combustion process [1–3]. Therefore, additional structures are introduced to enhance the mixing of the normal jets on the flat wall, and the backward-facing step (BFS) is one of the common structures in engineering. The appearance of the step causes a large-scale low-speed recirculation zone, and the jet behind it is affected in a complex manner. Moreover, geometrical parameters may determine the effect of the step.

The transverse jet in supersonic crossflow is a simple configuration that enhances mixing. There are four types of coherent structures observed in this configuration: The jet-shear layer vortices, the counterrotating vortex pair (CVP), the horseshoe vortex, and the downstream wake vortices. Gao et al. [4] and Lazar et al. [5] found that the near-field mixing is dominated by convection transport driven by large-scale vortices, while the far-field mixing is controlled by mass diffusion. The mixing process is mainly controlled by these coherent structures, where many factors are involved. Yang et al. [6] visualized the trajectory of jets with various injection angles and pressures based

on schlieren technology. A fitting curve was obtained to establish the quantitative relationship between the injection performance and the influential factors. Huang [7] investigated the molecular weight and injector configuration effects on the transverse injection flow. The results obtained by Reynolds-averaged Navier–Stokes (RANS) showed that the case with the equilateral triangular injector has the highest mixing efficiency and the larger molecular weight of the injectant can enhance the mixing slightly. Hariharan et al. [8] changed the inlet Mach number and inlet stagnation temperature in a numerical investigation and concluded that increasing the Mach number resulted in better mixing. When enhancement devices are installed in a transverse jet combustor, the flow structure is more complex.

There are many studies focusing on transverse jet schemes that adopt different mixing enhancement devices, such as struts [9,10], ramps [11,12], pylons [13,14], and cavities [15,16]. Unfortunately, the effect of the BFS on the transverse jet mixing in supersonic crossflow has not been thoroughly and systematically investigated. McDaniel [17] employed laser-induced fluorescence (LIF) in three injection configurations: Transverse jet, single injection behind the BFS, and staged injection behind the BFS. The reported data were fitted to quantitatively describe the effect of a rearward step. Karagozian et al. [18] used planar laser-induced fluorescence (PLIF) to visualize the transverse jet injected behind a backward-facing step and explored parametric studies about injection locations. The obtained jet structure and penetration depth showed that the penetration can be enhanced when the injection position is within the recirculation zone, but this enhancement is not obvious when the injection position is outside the recirculation zone. Kuratani et al. [19] investigated the mixing characteristics of transverse injection into a supersonic backward-facing step flow by particle image velocimetry (PIV). The growth rate of the mixing layer thickness was estimated by streamlines and the obtained root mean square (RMS) streamwise velocity and vorticity suggested effective mixing enhancement due to the vortices of all sizes.

Sharma et al. [20] used Menter's shear-stress transport (SST) model in the computational fluid dynamics (CFD) solver to perform the 3-D Reynolds Average Navier-Stoke (RANS) method on configurations in which jets were placed at various locations downstream of the step. The author indicated that mixing is strongly affected by the distance between the steps and the jet. The optimal location for the jet is the tail of the recirculation region behind the BFS. Then, a second jet was placed at various locations downstream, and it was concluded that the spacing between the jets is significant in determining the mixing performance [21]. Wu et al. [22] applied both numerical and experimental methods to study the flow structure of a transverse jet injected at different flow rates after a backward-facing step. The results showed that due to the large-scale recirculation zone, the upstream side of the barrel shock is weakly compressed, and the jet can enter the recirculation zone. Besides, the mixing enhancement is related to the jet to free-stream momentum, and the growth of the jet mixing layer with a large jet to free-stream momentum can be maintained to a more downstream position. Liu et al. [23] applied both the RANS method and a large eddy simulation (LES) to simulate supersonic flow over a backward-facing step and found that the step height has a substantial effect on flow patterns. Therefore, it is reasonable to believe that steps of different heights will have different effects on the downstream jet.

Therefore, knowledge about the influence mechanism of the BFS on the jet and geometric parameter effect is limited. In engineering applications and design optimization, these problems are the key ones for fully exploiting the performance and for guaranteeing the stability and reliability. The purpose of this numerical study was to gain an in-depth understanding of the mechanism of the interaction between the BFS and the transverse jet, to evaluate the effect of the step on the mixing characteristics, and to summarize the rule of this effect on the step depth.

The numerical model and method are introduced firstly, and then code validation is conducted based on the experiments by Santiago and Dutton [24]. Afterwards, the results obtained from LESs applied at different step heights (0, 1D, 1.58D) are discussed and analyzed. Finally, some valuable conclusions are summarized.

2. Models and Methods

Experimental studies are often performed to understand physical phenomena and to support CFD verification. However, the flow field information obtained by experiments is very limited, which hinders the application of experimental data in practical engineering designs. With the rapid development of computer technology, computational research has increasingly been conducted. Numerical simulations are a potential new tool for future designs. Hassan et al. [25] reviewed the computational models applied to supersonic transverse jets and concluded that LESs are capable of capturing large-scale turbulent structures and are not as computationally expensive as the direct numerical simulations (DNSs). Therefore, the LES method is selected to study the mixing characteristics of air injected normally from the wall downstream of the BFS. This section describes the models and numerical methods adopted by the LES.

2.1. Governing Equation and Turbulence Model

For a supersonic flow, the LES solves the Favre filtered compressible Navier–Stokes (N-S) equations. In the paper, the three-dimensional nonreactive flow needs to be solved, and the conservative governing equations are written as:

$$\frac{\partial \mathbf{Q}}{\partial t} + \frac{\partial \mathbf{E} - \mathbf{E}_v}{\partial x} + \frac{\partial \mathbf{F} - \mathbf{F}_v}{\partial y} + \frac{\partial \mathbf{G} - \mathbf{G}_v}{\partial z} = \mathbf{S}, \tag{1}$$

where $\mathbf{Q}$ represents a vector of conservative variables; $\mathbf{E}$, $\mathbf{F}$, and $\mathbf{G}$ are vectors of inviscid fluxes; and $\mathbf{E}_v$, $\mathbf{F}_v$, and $\mathbf{G}_v$ are vectors of viscous fluxes in three directions, and the specific form of flux has been defined in previous studies [26,27]. $\mathbf{S}$ represents the chemical reaction source term, which is 0 for a cold flow.

In the LES method, the Yoshizawa subgrid-scale (SGS) model [28] is used to model the turbulent kinetic energy that cannot be solved with the grid. The subgrid-scale turbulent kinetic energy is transported according to the following equation:

$$\frac{\partial(\overline{\rho}k^{sgs})}{\partial t} + \frac{\partial\left(\overline{\rho}k^{sgs}\widetilde{u}_j\right)}{\partial x_j} = \frac{\partial}{\partial x_j}[\overline{\rho}(\nu + \frac{\nu_t{}^{sgs}}{\mathrm{Pr}_t})\frac{\partial k^{sgs}}{\partial x_j}] + P_k{}^{sgs} - D^{sgs} \tag{2}$$

where $P_k{}^{sgs} = -\tau_{ij}{}^{sgs}\left(\partial\widetilde{u}_i/\partial\widetilde{x}_j\right)$ denotes the production of k^{sgs}; $D^{sgs} \approx C_d\rho(k^{sgs})^{2/3}/\Delta$ is the dissipation term; and $C_d = 0.1$.

2.2. Turbulence Inflow Generation Technique

It is necessary to supply the turbulent inlet boundaries so that the LES can directly solve large-scale turbulent structures. The recycling/rescaling generation method [29] is an effective way to provide turbulent inlet conditions for the LES. In this paper, the method is used to generate the turbulent inlet boundary condition.

2.3. Numerical Schemes

The governing equation is solved based on the finite difference method. The 5th-order weighted essentially nonoscillatory (WENO) scheme and the 2nd-order central difference scheme are adopted to the space derivative term. Considering the need to solve nonsteady problems, a second-order dual time-step approach is implemented for time advancing. The lower-upper symmetric Gauss–Seidel (LU-SGS) method is selected for inner iteration.

2.4. Computational Grids and Conditions

A baseline case is based on the experiments by Santiago and Dutton [21], where the inlet Mach number of the supersonic flow in the experiment is 1.6, the stagnation temperature is 295 K, and the stagnation pressure is 241 kPa. According to the adiabatic relationship formula, the corresponding

static temperature and static pressure can be obtained as shown in Table 1. A circular injection with a diameter of 4 mm is installed on the flat plate, and the air with a total pressure of 476 kPa and a total temperature of 300 K is injected through the circular hole vertically. It is important to note that although the other parameters are consistent, the incoming Reynolds number used in the simulation is only 1/6 of its experimental value in order to reduce the number of grids. The treatment does not have a large impact on the mixed flow field [30], and this strategy has been adopted in the previous LES [31]. To study the BFS effect, two steps with different heights are designed for installation in the baseline case. The above conditions are used in simulations for the configurations with three different heights of the step.

Table 1. Conditions of crossflow and jet in the experiment [24].

	Crossflow	**Jet**
Ma	1.6	1.0
P (kPa)	56.7	251.46
T (K)	195.1	250.0
D (mm)	4	
J	1.7	

A schematic of the computational domains for these configurations is shown in Figure 1. The position and configuration of the steps are shown in Figure 1, and the heights are given in Table 2. The origin of the coordinate system is set at the center of the jet inlet. In the focus area, the grid is refined, and buffer zones are settled near the downstream, left, right, and top exits, where the grid is gradually stretched. Grid points within the boundary layer are refined to ensure that the height of the first-layer grid satisfies $y^+ = 1$. The first-layer grid away from the wall is set to 0.006 mm. Exhaustive mesh information is listed in Table 3. The inlet adopts the "recovery/regulation" method to generate a fully developed supersonic turbulent boundary layer; the lower wall is adiabatic, with a non-slip and non-penetration wall; the jet inlet velocity, temperature, and pressure are specified according to the experimental conditions; and the remaining boundaries are set to the supersonic outlet condition.

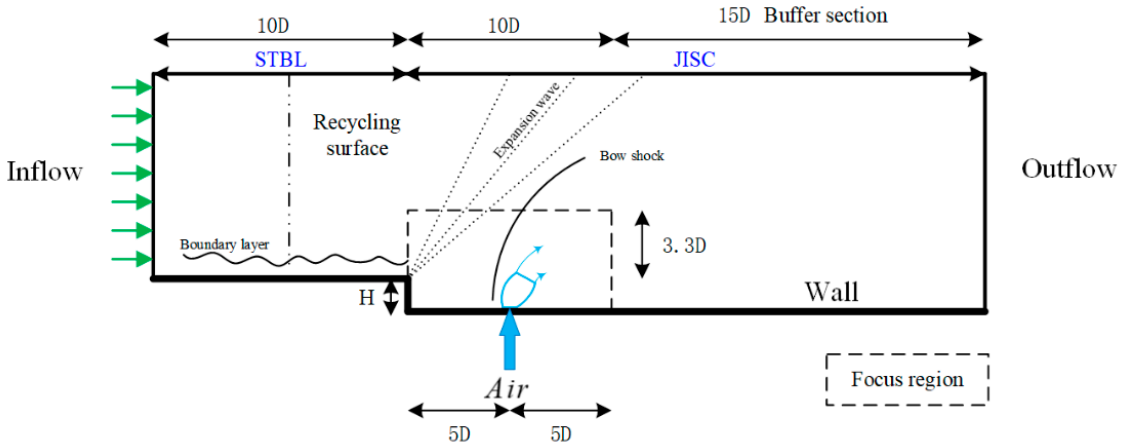

Figure 1. Schematic of the computational domain for the case with different step heights.

Table 2. Step height of different cases.

Case Number	**H**
Case 1	0
Case 2	1D
Case 3	1.58D

Table 3. Grid number in the computational domain and corresponding resolution in the focus region.

Case	N_ξ	N_η	N_ζ	Total (Million)	$\Delta_\xi{}^+$	$\Delta_\eta{}^+$	$\Delta_\zeta{}^+$
Case 1	721	181	181	23.6	20	1–20	20
Case 2	721	181 (STBL) 236 (JISC)	181	27.6	20	1–20	20
Case 3	721	181 (STBL) 251 (JISC)	181	28.7	20	1–20	20

3. Validation

Before analyzing the results, the numerical simulation method needs to be validated for its reliability. To validate the results in the present study, the velocity profile at different locations was first compared with the experimental results [24] and a published LES one [31]. The velocity field is the basic characteristic of the flow field, and it is fundamental to drive the mixing of the jet and the incoming flow. Figure 2 shows the comparison of the experimental and numerical flow velocity curves at different positions on the center section. At 2D downstream of the jet, the distinction of the flow direction velocity obtained by the LES is large, especially in the near-wall area and in the jet wake area. This phenomenon is less severe at the downstream positions, where x = 3D, 4D, and 5D. This observation shows that the present LES predicted a near-wall low velocity region, which is not shown by the experiment. The LES performed by Kawai reported a similar underestimation of the streamwise velocity near the wall at x/D = 2. The factors could be contributed by the different conditions (e.g., turbulence levels) of the jet inlet in the experiment and simulations. Simultaneously, the error of experimental measurement may also be one of the reasons.

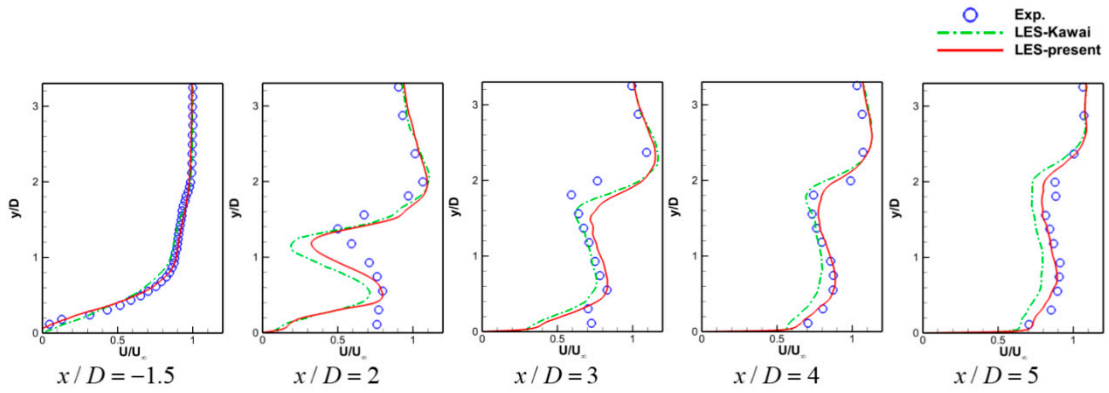

Figure 2. Comparisons of the mean streamwise velocity U/U_∞ profiles between the LES and the experimental data at x/D = −1.5, 2, 3, 4, and 5; solid lines: LES, dotted line: Kawai's LES, circle symbols: Experimental.

The same comparison was made with the normal velocity, and the result is shown in Figure 3. Overall, the normal velocity matches the experimental values better than the streamwise one. The normal velocity of the jet wake is slightly underestimated. This reflects that the CVPs captured by the LES are stronger than those in the experiment and induce a larger upward normal velocity. Comparisons of the streamwise and wall-normal velocities between the present LES and Kawai's LES at the midline plane of z/D = 0 are shown in Figure 4. Regarding streamwise velocities, the absolute value of the negative velocity in the blue area upstream of the jet is small, indicating that jet expansion is not as rapid as in the other LES. In terms of the wall-normal velocities, the results of the two simulations are in good agreement. Figure 5 shows the distribution of the wall static pressure along the flow direction at different spanwise positions (z/D = 0, 2). The difference between the experimental data and the simulation results is positive upstream of the orifice and negative downstream of the orifice, but the deviation is relatively small.

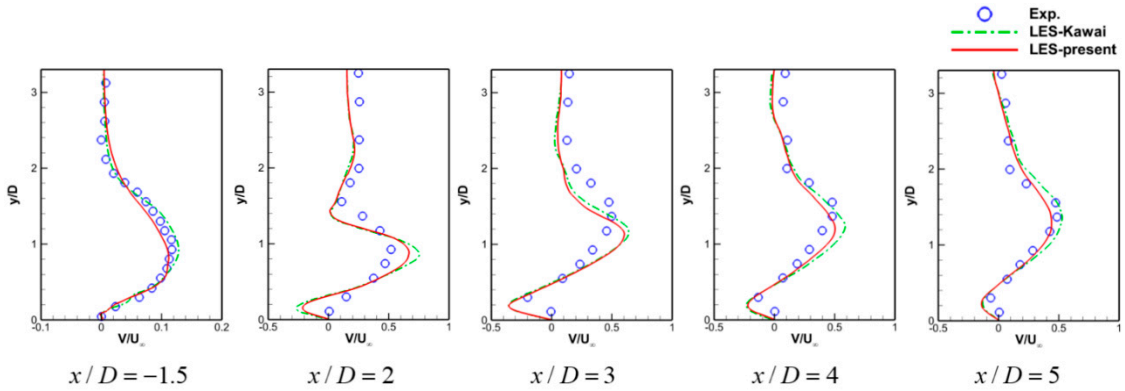

Figure 3. Comparisons of the mean wall-normal velocity V/U_∞ profiles between the LES and the experimental data at x/D = −1.5, 2, 3, 4, and 5; solid lines: Present LES, dotted line: Kawai's LES, circle symbols: Experimental.

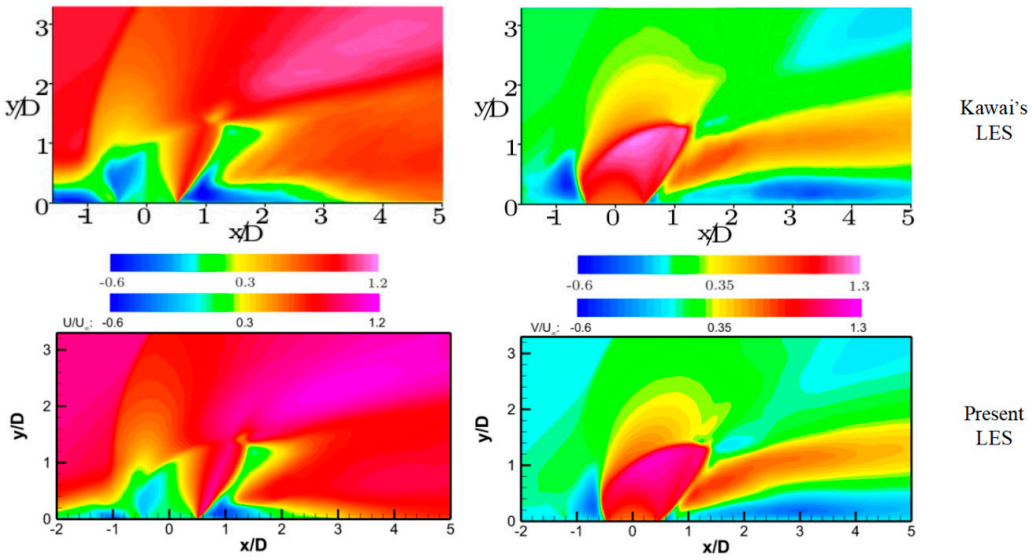

Figure 4. Streamwise and wall-normal velocities, U/U_∞ and V/U_∞, at the midline plane of z/D = 0. The top two results are the LES results published by Kawai in [31], the bottom two results are the present LES results.

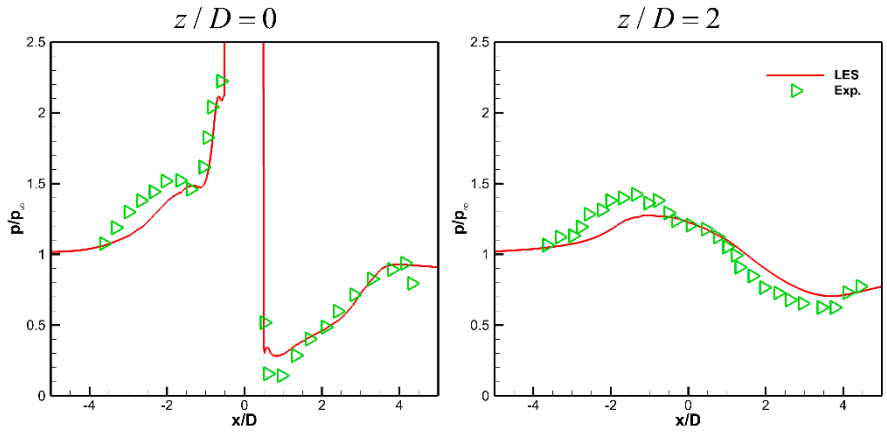

Figure 5. Comparisons of the mean wall-pressure p/p_∞ distributions between the LES and the experimental data at z/D = 0 and 2; solid lines: LES, ▷: Experimental.

In general, there are some errors in the quantitative comparison between the results of this paper and the experiment; considering the error of the experimental data itself and the limitations in the

simulation implementation, these errors are acceptable. Moreover, a comparison with the existing LES results reveals that the LES solver in this paper is also reliable.

4. Results and Discussion

In this section, the obtained flow field is analyzed, and the distributions of the velocity and pressure and the shapes and positions of the shocks and vortex structures are compared. Furthermore, the mixing characteristics caused by the interaction of the transverse jet and main flow with different step heights are compared. Finally, the effects of the step height on the mixing efficiency and the penetration depth of the jet are summarized.

4.1. Flow Structure of the Transverse Jet under the Effects of the BFS

The left side of Figure 6 shows the Mach number distribution at the central slice (z/D = 0), which is also superimposed on the streamline in the plane, and the green line indicates the sound velocity contour. Shown in the figure, the range of the subsonic region is significantly expanded due to the presence of steps, and the leeward zone is dominated by subsonic conditions in case 3. The subsonic zone delays the change of the jet velocity direction, which is beneficial for the jet to more deeply enter the mainstream. When the wall surface is a flat plate, a separation area before the jet is caused by the negative pressure gradient; when a backward step is added, the step separates the upstream boundary layer and creates a large-scale recirculation zone. The separation bubble in front of the barrel shock wave becomes larger also. A wide range of subsonic regions and recirculation regions affect the expansion and penetration behaviors of the jet. Simultaneously, the recirculation regions lead to differences in the shock system and vortex structure, thus affecting the local and overall mixing performance. The right side of the figure exhibits the normal velocity with streamlines in the axial planes. The CVPs in the leeward region are found in all cases, but there is only a small near-wall wake vortex in cases 2 and 3. In the baseline case, the CVPs gradually lift along the flow direction, while the lift in cases 2 and 3 is not obvious. The position of the vortex pair is closer to the wall surface in the case with a BFS, and its range is larger. Thus, more fuel is involved in the region near the wall. Due to the lack of induction of turbulent boundary layer separation before the injection port, wake vortexes near wall are weakened in cases 2 and 3.

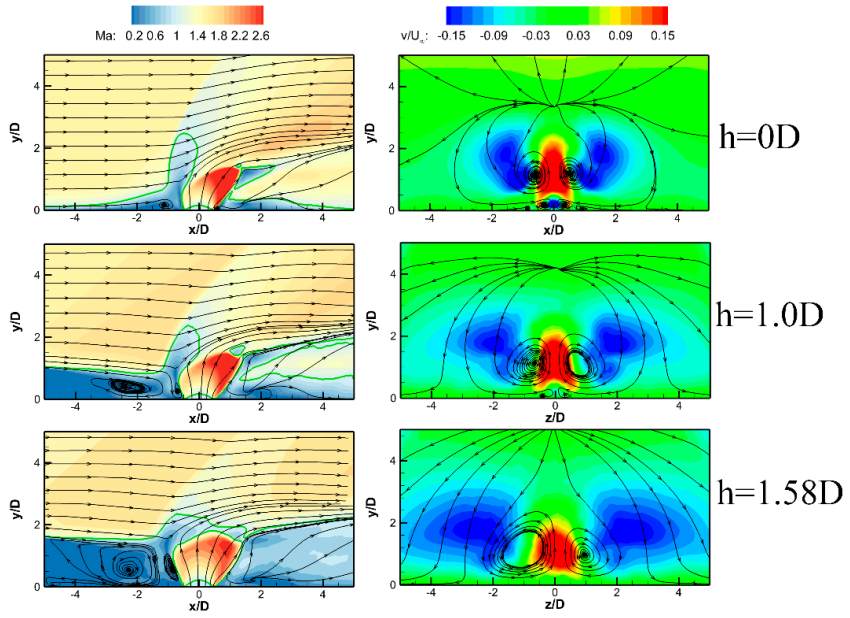

Figure 6. Comparison of the center-plane Mach number with streamlines for cases 1, 2, and 3 (**left**) and the normal velocity with streamlines in axial planes x/D = 4 (**right**).

After being injected, the jet is forced to turn by the momentum of the incoming flow and form a barrel shock. The turning process is also accompanied by the expansion of the high-pressure jet in the ambient pressure environment. The steps create a subsonic separation zone upstream of the jet (see Figure 6) and reduce the static pressure in this zone. As shown in Figure 7, the pressure distributions upstream of the jet at the central plane in the three cases are significantly different. Due to the formation of the separation zone and separation shock, the pressure on the upstream side of the orifice is approximately 1.5 times higher than the incoming flow pressure. In cases 2 and 3, the pressure in front of the injection hole is basically the same as the pressure in the separation zone caused by the step, which is slightly lower than the incoming flow pressure. Therefore, the jet will expand more vigorously, forming a higher barrel shock. The solid black line in Figure 7 is the streamwise velocity isoline $\left(u/u_\infty = 1 \times 10^{-5}\right)$, which is used to identify the location of the recirculation zone. There are two characteristic recirculation zones in all three cases, of which the downstream recirculation zones have similar shapes and positions. The recirculation range induced by the step is larger than that caused by the wall separation. Since the recirculation zone is subsonic, the bow shock is lifted from the bottom wall with the step depth increased.

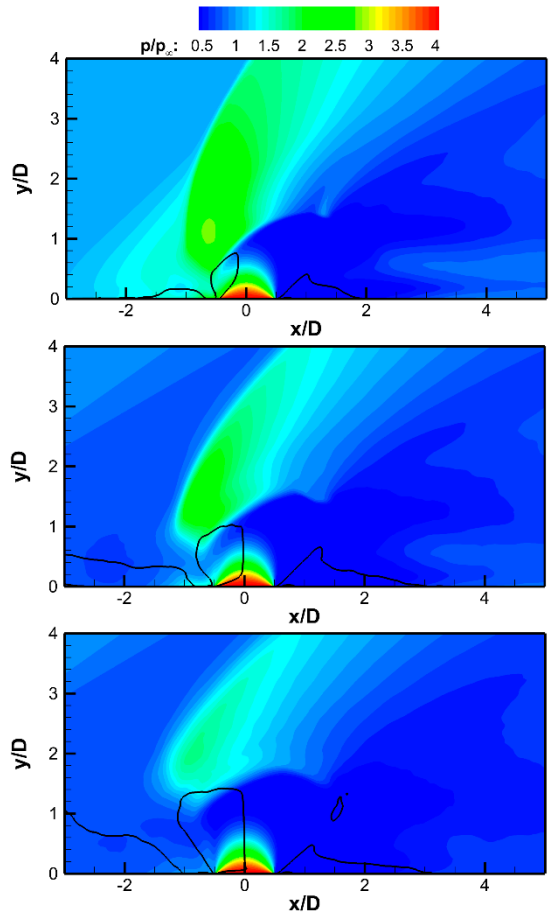

Figure 7. Pressure p/p_∞ contours with the isoline $(u/u_\infty = 1 \times 10^{-5})$ in the centerplane for cases 1, 2, and 3.

Figure 8 gives another perspective to observe the recirculation zones and pressure distribution. The figure shows the top view of the isosurface of the flow velocity $(u/u_\infty = 1 \times 10^{-5})$ colored by the pressure and draws the streamlines that bypass the recirculation zone. The upstream crescent-shaped recirculation zone is greatly expanded in cases 2 and 3. Since the recirculation is not caused by the boundary layer separation, its pressure gradient is also smaller than that in case 1. The range of the downstream λ-shaped separation zone also becomes larger with the step height increased. In Figure 8,

the streamlines marked by squares are controlled by CVPs, and those marked by circles are controlled by wake vortices. Because the wake vortex is weakened by the steps, the streamline is not affected by the wake vortex in case 3. A wide range of CVPs and recirculation zones allow more fuel to enter the near-wall zone, which is highly beneficial for stable combustion in the near-wall zone.

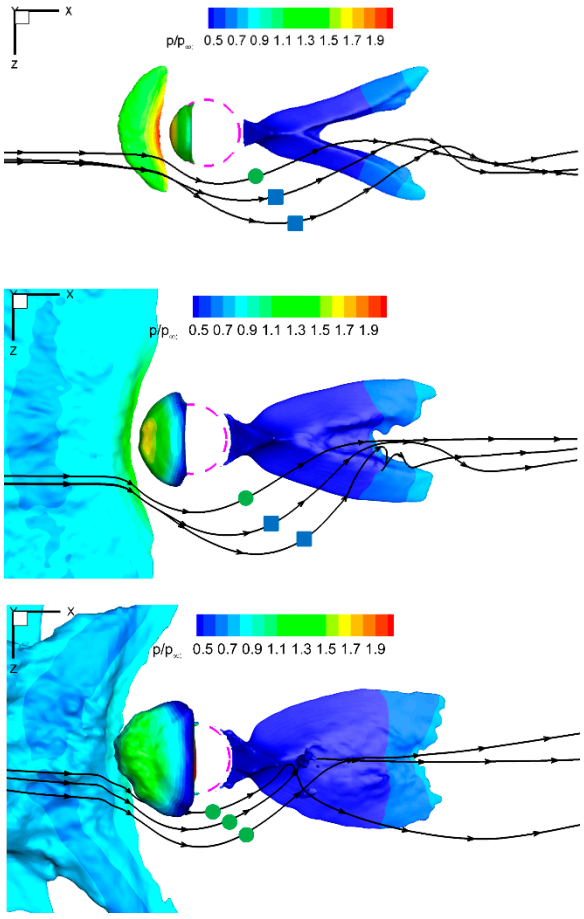

Figure 8. Top view of the isosurface of the flow velocity ($u/u_\infty = 1 \times 10^{-5}$) colored by the pressure contour and overlapped by streamlines bypassing the recirculation zone.

By analyzing the velocity and pressure distributions in the flow field, the configuration with steps will produce a large-scale recirculation zone, which has a significant impact on the flow field structure. The most important factors controlling the mixing process are the shear vortex on the windward side and the CVPs on the leeward side. Analyzing the effect of steps on these large-scale structures is important for understanding how the step effect qualitatively changes the mixing results under similar mixing mechanisms.

The instantaneous 2-D flow features at the midline plane are visualized by the density gradient magnitude in Figure 9. There is no turbulent boundary layer formed on the wall behind the step in cases 2 and 3, and the step shear layer seems to act as a boundary layer. The bow shock formed by jet blocking intersects with the shear layer and the intersection lifts as the step depth increases. At the same time, the angle between the bow shock and the wall decreases. The barrel shock is obviously different in shape among the three cases, forming a different Mach disk. In Figure 9, the angle between the central axis of the barrel shock (red dotted line in the figure) and the wall increases with the height of the step, from 67.6° to 82.9°. This means that the velocity of the jet remains upward for a longer time, and the jet can penetrate deeper in Cases 2 and 3. Shear vortices generated by the Kelvin–Helmholtz (K-H) instability exist after bow shock, which originates from the height of the intersection of the bow shock and shear layer (the boundary layer in case 1). This height also increases as the steps deepen.

In addition, due to the existence of the step recirculation zone, there is no boundary layer separation upstream, so there is no separation shock in cases 2 and 3.

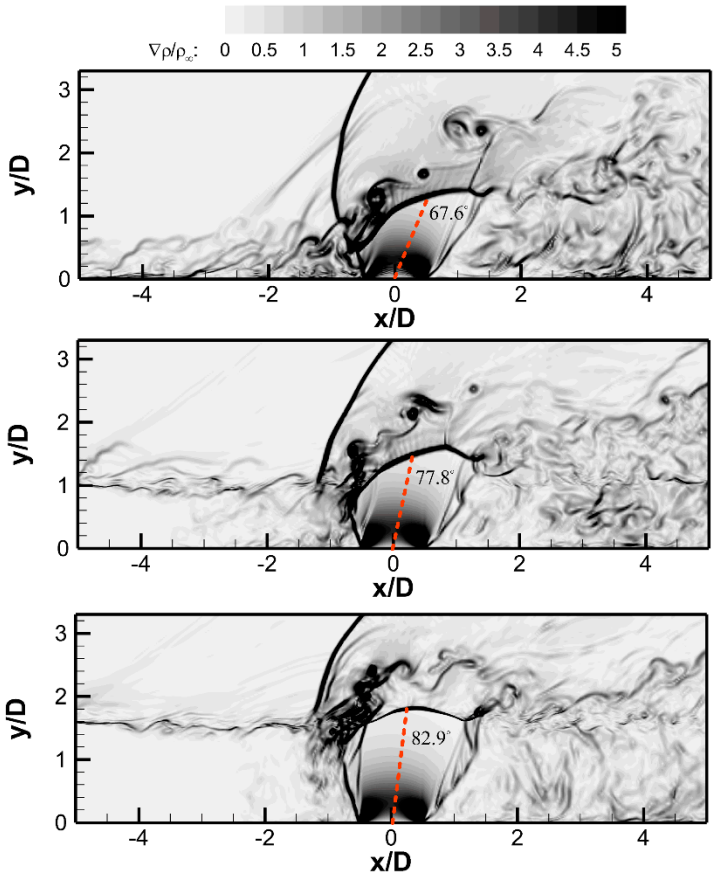

Figure 9. Instantaneous snapshots of the density gradient magnitude at the midline plane of z/D = 0.

Turbulent vortices play an important role in the mixing process, especially the shear vortex on the windward surface, which dominates the near-field entrainment-stretching-mixing process. To show the three-dimensional structure of the vortex, Figure 10 shows the mixture fraction isosurface colored by the vorticity magnitude and the λ_2 isosurface colored by the streamwise velocity. According to the isosurface of the mixture fraction (left side), the windward surface of the jet folds and rolls up large-scale eddies due to the K-H instability. As the large-scale recirculation zone formed by the steps rises, the upwind shear vortex appears farther away from the wall at a smaller scale. Observing the vorticity distribution on the isosurface, the region of high vorticity caused by the strong shear at the jet exit is gradually dispersed. Under the influence of larger-scale CVPs, the vorticity of the downstream near-wall area is stronger, which is beneficial for mixing in the leeward area. The right figure shows the hairpin vortex of the boundary layer/shear layer and the vortex tube of the jet in the windward region by using the λ_2 criterion. Under basic conditions, the vortexes in the near field are larger because of the stronger shear, and it gradually breaks down to form smaller-scale vortexes. The streamwise velocity distribution on the surface of the vortex tube indicates that the velocity in cases 2 and 3 is lower, which is closer to the mainstream velocity, and the shear is weaker than in case 1. Therefore, the step weakens the shear of the jet outlet, and the vorticity scale in cases 2 and 3 is small.

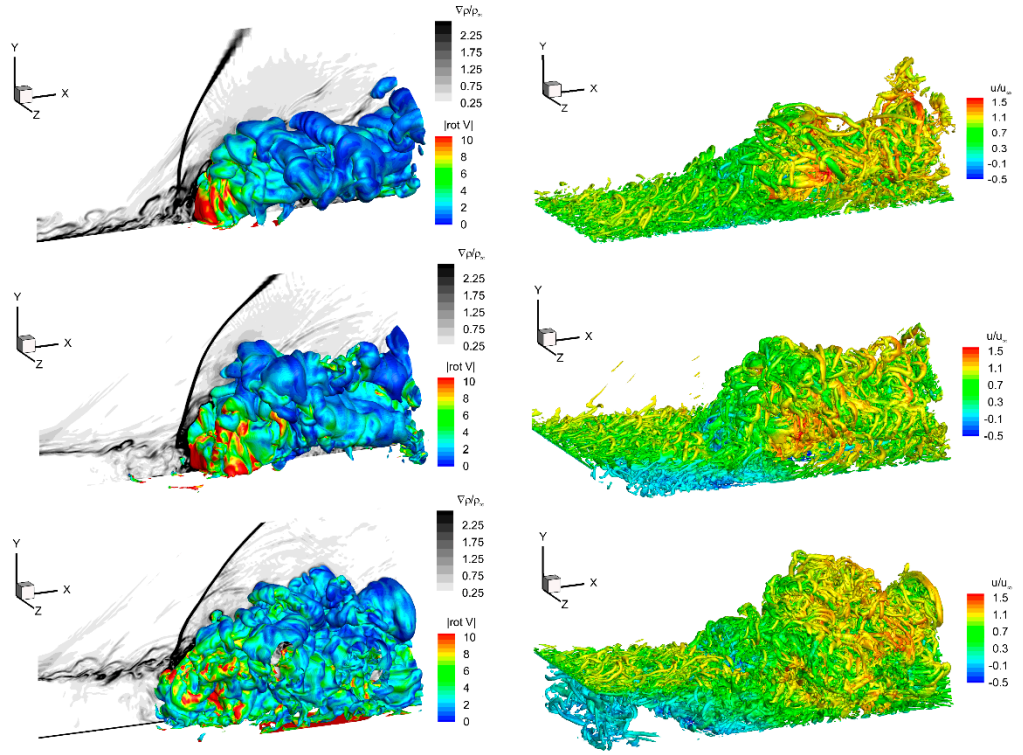

Figure 10. Instantaneous snapshots of vortex and jet structures: (**a**) isosurfaces of the mixture fraction Y = 0.2 colored by the vorticity magnitude; (**b**) isosurface of $\lambda_2 = -0.5$ colored by the streamwise velocity.

The two-time two-point correlation [32] of the injectant mass fraction fluctuation is defined to describe the convection of the windward large-scale structure:

$$r_{s,t}(x, y, \Delta t) = \frac{(1/N)\sum_{i=1}^{N}\left[Y''(x_{ref}, y_{ref}, t)\cdot Y''(x, y, t+\Delta t)\right]}{Y''_{rms}(x_{ref}, y_{ref})\cdot Y''_{rms}(x, y)} \tag{3}$$

Here Δt is fixed at 0.535 ms and (x, y) is taken as the points located at the grid node on the central plane. The initial reference point $\left(x_{ref}, y_{ref}\right)$ is set to the position of the 50% maximum jet mass fraction at x/D = 0. Then, the position (x_{max}, y_{max}) where the correlation coefficient $r_{s,t}(x, y, \Delta t)$ takes the maximum value is used as the next reference point. The convection of the large-scale structure can be tracked in this way. The convection velocity can be estimated as follows:

$$U_c = \frac{\sqrt{\left(x_{\max} - x_{ref}\right)^2 + \left(y_{\max} - y_{ref}\right)^2}}{\Delta t} \tag{4}$$

Figure 11 plots the coherent structure traced from the initial position, marked by the correlation coefficient contour of the spindle shape. The dotted lines indicate the maximum (green), 50% (blue), and 10% (red) averaged injectant mass fraction tracks, respectively. The coherent structure development and downstream transport between the maximum track and the 10% track are shown. During downstream transport, the coherent structure is stretched by the shearing of the velocity gradient. Under the action of the step recirculation zone, the shear layer on the windward surface is thicker, the velocity gradient is smaller, the stretching effect is weaker, and the coherent structure can be maintained in an approximately circular shape. As the depth of the steps increases, the wider distance between the maximum track and the 10% track also shows that the steps enhance the mixing

and penetration of the windward side of jet. Figure 12 shows the convection velocity estimated by Equation (4). Near the orifice of the injector, the convection velocity is close to the jet velocity and then begins to accelerate. In general, as the steps increase, the convection velocity decreases, which may provide a longer mixing time and postpone local blending.

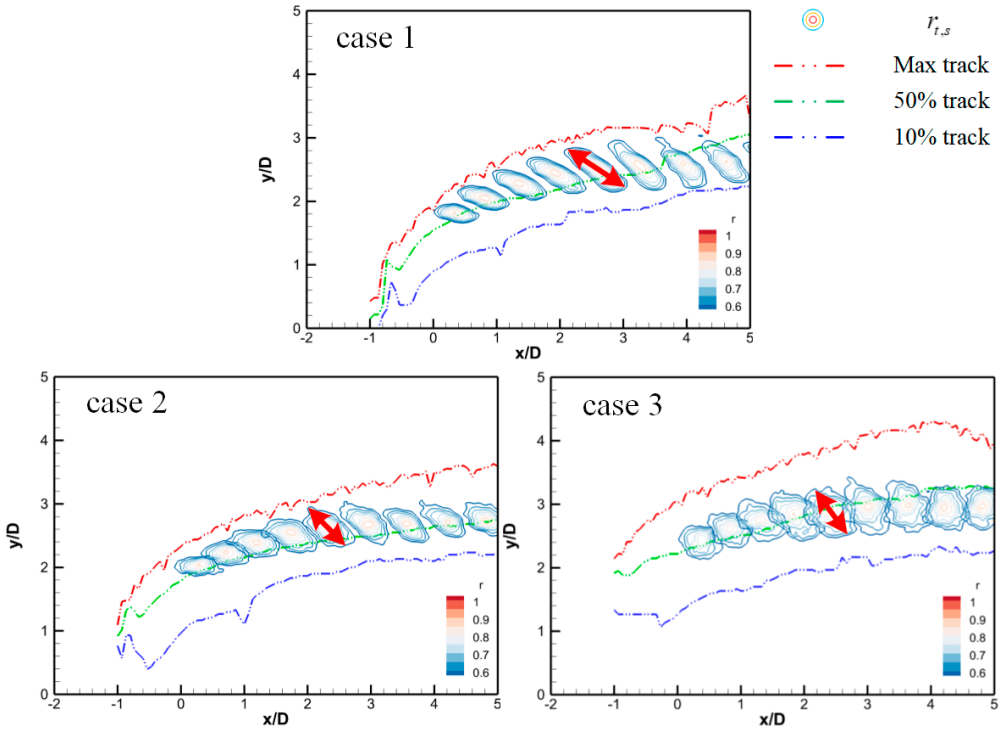

Figure 11. Tracks of windward large-scale structures with the correlation coefficient $r_{s,t}$.

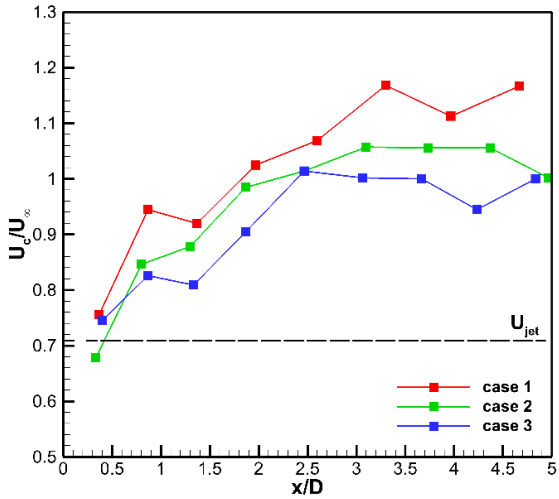

Figure 12. Convection velocity of windward large-scale structures; red line: Case 1, green line: Case 2, blue line: Case 3.

Figure 13 is a schematic diagram of the flow field structure of the transverse jet in the backward step configuration. The supersonic flow forms a turbulent boundary layer on the upstream wall of the step. The wall is interrupted at the step, and a series of Plant-Meyer waves are generated at the sharp corner. Then, the boundary layer is separated, and a large-scale recirculation zone is formed after the step. The jet is injected at the vertical speed of the wall and accelerates and expands forcefully. Then, the jet is compressed by the incoming flow to form a barrel shock wave and a Mach disk. Due to the presence of the step recirculation area, the location of the barrel shock rises, and the corresponding bow

shock is also located farther away from the wall. The supersonic flow and the transverse jet interfere with each other, inducing counter-rotating vortex pairs (CVPs) in the wake of the jet; meanwhile, the wake vortex is weakened by the effect of the steps, so that the CVP controls a larger area, including the near-wall zone. The windward side of the jet is induced by K-H instability, forming a large-scale shear vortex. As the thickness of the recirculation zone increases, the position of the vortex increases accordingly. However, due to the weakening of the shear, the scale and convection velocity of the vortex with the action of the step decrease.

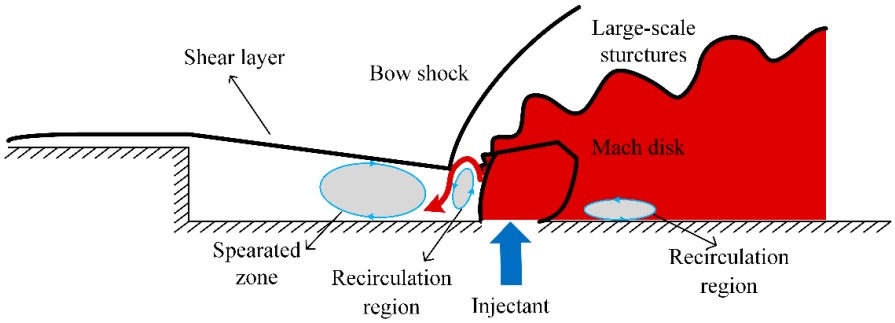

Figure 13. Schematics of the transverse injection of an under-expanded jet into a supersonic crossflow with the effect of the BFS.

4.2. Mixing Characteristics with Different Step Heights

The influence of large-scale recirculation in the velocity distribution, shock wave, vortex shape, and position around the jet is described above. The mixture fraction used to characterize the local mixing degree of the jet and main flow is mainly controlled by the coherent structure in the near field. Therefore, step recirculation can result in different mixture fraction distributions. The first column in Figure 14 shows the time-averaged distribution of the mixture fraction at the midline plane of z/D = 0. The solid lines depict the profile of the jet with the mixture fraction isoline (Y = 0.1 black line; Y = 0.5 purple line; Y = 0.9 white line). The time-averaged mixture fraction distribution reflects that the step strengthens the overall mixing effect. Additionally, the deeper the step is, the more obvious the effect. The black line indicates that the jet can enter the mainstream in a wider manner and has a greater distribution in the near-wall area upstream and downstream for case 3. The widening of the distance between the three isolines indicates that the local mixture fraction gradient decreases.

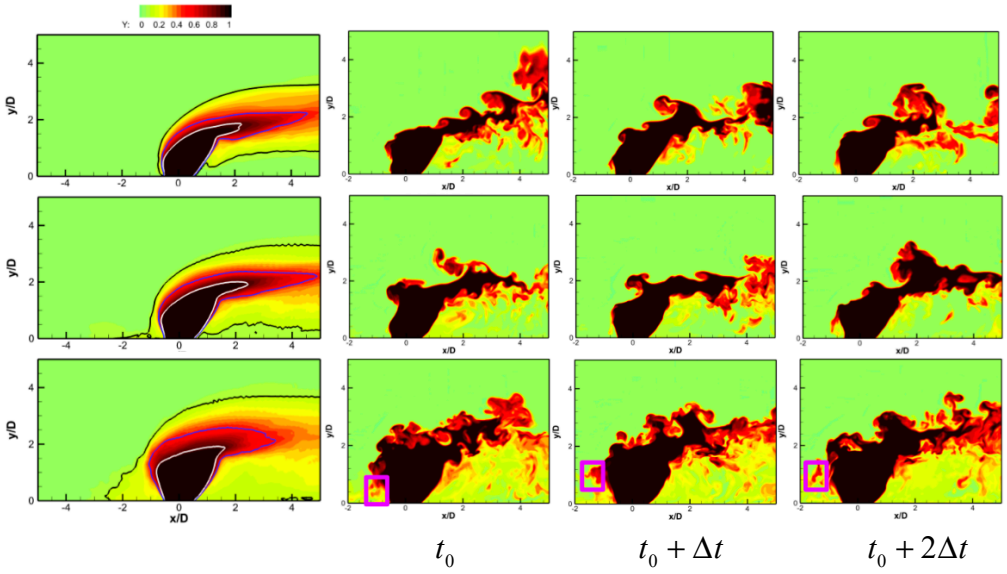

Figure 14. Time-averaged and instantaneous mixture fraction at the midline plane of z/D = 0.

The shape and position of the vortex evolve with time, and the mass fraction distribution of the jet also changes due to vortex driving. The three columns on the right side in Figure 14 establish three instantaneous mixture fraction contours at different instants ($\Delta t = 2.6756ms$), which shows the process of the shear vortex roll-up and fall-off events on the windward side. First, the location of the origin of the vortex is different in the three cases, which is in accordance with the aforementioned observation. Note that as marked by the purple box, the jet can enter the large-scale recirculation zone upstream with the effect of two recirculation zones for case 3. The smaller counterclockwise separation zone in front of the barrel shock wave rolls out the jet and then throws it to the front side of the separation zone. It then enters the range of the clockwise step recirculation zone and can be entrained downward by the recirculation.

As mentioned above, the step effect accelerates the mixing process. It means that at different step depths, the distribution of the mixture fraction in the same flow direction position should be different. Figure 15 shows this difference by superimposing the instantaneous and time-averaged results of the mixture fraction at x/D = −1, 1, 3, and 5. The outermost time-averaged contour indicates the change in the flow direction of the penetration depth. The spread range obviously increases with the step height. In case 1, the jet profile shows a significant lift, while in cases 2 and 3, the fuel distribution range in the near-wall area is greater than that when there is no step, and the lift is not obvious. Another difference is the mixture fraction of the jet upstream, which is shown in the first column in Figure 15. More injectant enters the area upstream of the jet, and the distribution range is larger when the step height increases. In case 3, the upstream jet distribution is concentrated near z/D = 0, and the range is very narrow.

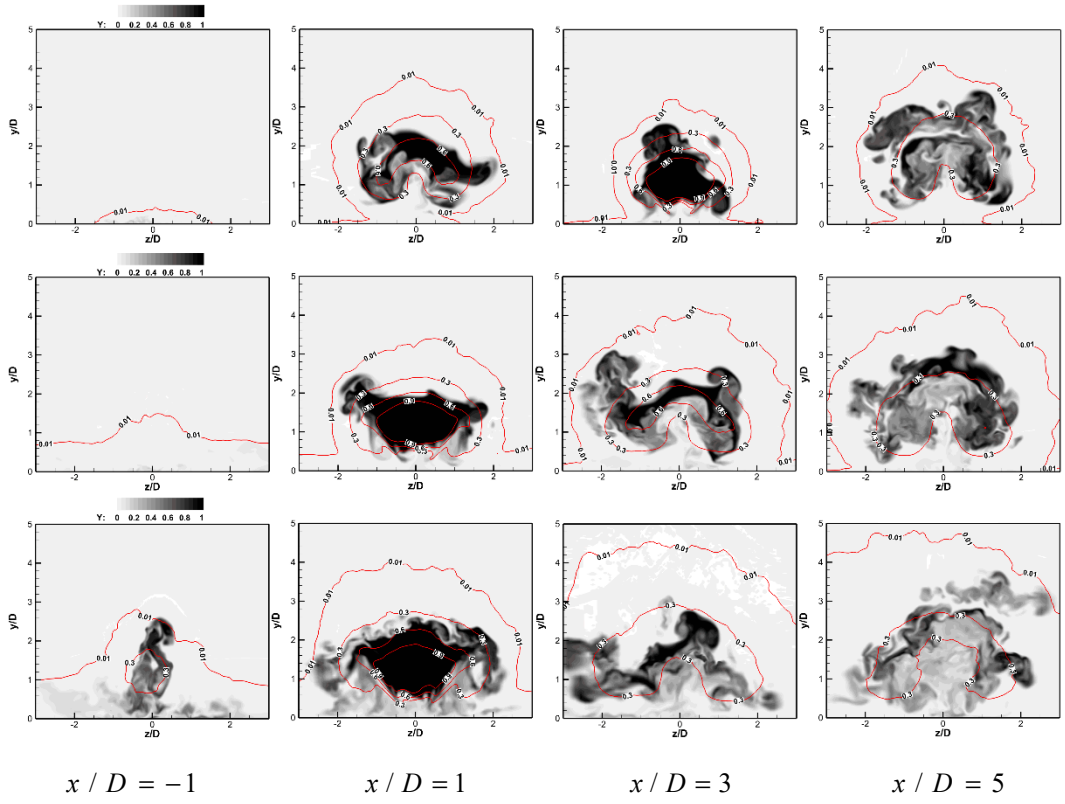

Figure 15. The instantaneous mixture fraction at downstream positions x/D = −1, 1, 3, and 5 overlapped with the time-averaged mixing fraction isoline.

To quantitatively analyze the intermittency of jets observed in Figures 14 and 15, the probability density function (PDF) method was applied for data processing of the jet mass fraction. Figure 16 shows the probability density function, time-averaged, and standard deviation of the injectant mass

fraction at the central plane. The joint probability density function value of the position in the y direction and the mixture fraction is represented by the colorful contour. The time-averaged and the standard deviation profiles are indicated by a black solid line and a red broken line, respectively. The high probability area distributed at Y = 0 means the unmixed area, while the area distributed at Y = 1 indicates the jet core. Along the flow direction, the jet core gradually disappears, and the peak of the mean value also decreases. At x/D = 1, the standard deviation is bimodal. One appears in the windward area and the other is in the leeward area. Further downstream, the standard deviation approximates a Gaussian distribution and its peak value decreases.

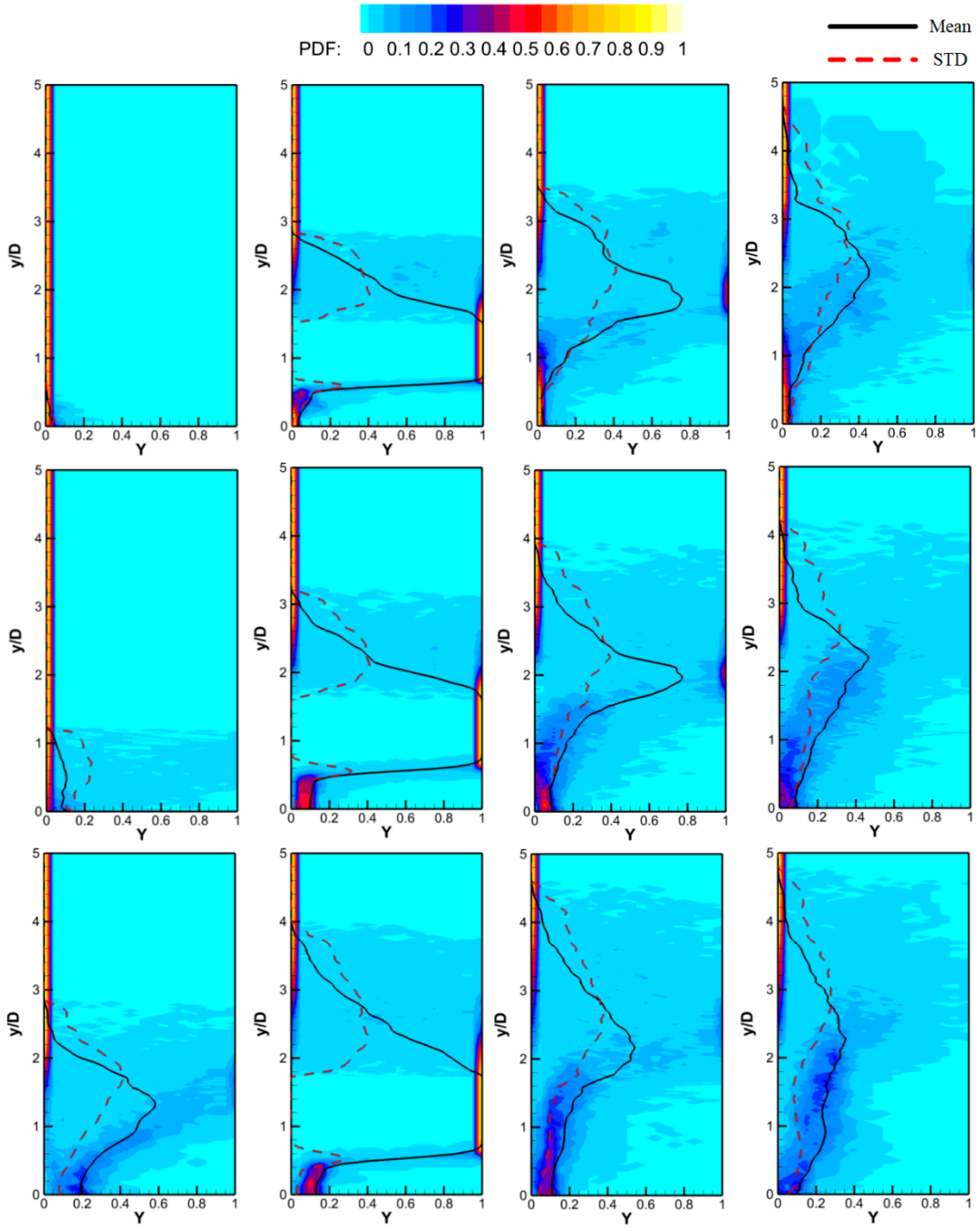

Figure 16. PDFs of the injectant mass fraction at x/D = −1, 1, 3, and 5 in the center plane. Mean: time-averaged profile; STD: Standard deviation profile.

Affected by the steps, the intermittency of the jet in the windward zone at the same flow direction position weakened, resulting in a reduction in the standard deviation value. However, the shear layer becomes thicker, so that the range of the standard deviation > 0 expands upward. The steps also changed the statistical characteristics of the mixture fraction in the leeward zone. The larger PDF values are distributed near the mean value, and the mean value increases with the height of the steps near the wall surface at all positions. Due to the upstream entrainment mechanism shown in Figure 14, the mixing of the jet at x/D = −1 is significantly enhanced with the effect of steps. In particular, in case 3 (H = 1.58D), there is a peak of the mean mixture fraction along the wall distance. The PDF value $(0 < Y < 1)$ concentrates at the branch below the peak point, and there is a strong intermittency on the other side of the peak. It is the result of vortex-driven blending.

The penetration depth and spread are important indicators used to describe the jet mixing behavior. Figure 17 plots the jet penetration depth and spread using the jet boundary definition Y = 0.01. Overall, as the step size increases, both indicators improve, and the expansion spread increases drastically. Additionally, the comparison shows that the difference in the initial value of the penetration depth (x/D < −1) in cases 1–3 is greater than the difference in the downstream x/D = 5. In other words, the steps only "raised" the jet, and the expanded jet weakened the penetration. Referring to Figure 15, a comparison of the spread reveals that with the effect of the step, the larger-scale CVPs control the jet mixing in a wider spread.

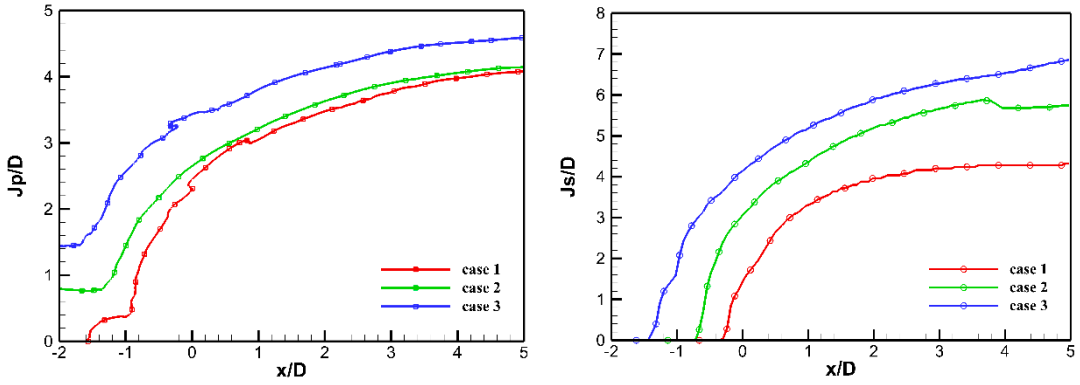

(**a**) (**b**)

Figure 17. Jet penetration depth (Jp in (**a**)) and spread (Js in (**b**)). (Y = 0.01 is set as the jet boundary).

The time-averaged mixing efficiency for the jets along the flow direction is used to evaluate the mixing performance. The mixing efficiency can be calculated as:

$$\eta_{ave} = \frac{\int \overline{\rho u}\overline{Y}/\overline{\varphi}}{m_j} \qquad \overline{\varphi} = \begin{cases} 1 & (\varphi \le 1) \\ \varphi & (\varphi > 1) \end{cases} \tag{5}$$

where Y is the mass fraction of the jet, ρ is the fluid density, and u is the velocity. The m_j is the mass flow rate of the jet; and φ is the fuel equivalent ratio, which is calculated using ethylene as a substitute because its molar mass is similar to air.

The total pressure recovery coefficient is used to evaluate the total pressure loss during the mixing process:

$$\sigma_{rec} = \frac{\int P_0 \rho u dA}{\int P_{0,\infty} \rho u dA}, \tag{6}$$

where P_0 is the local total pressure and $P_{0,\infty}$ is the total pressure of incoming flow.

Figure 18 plots the integration result of Equations (5) and (6) in the x-plane along the flow direction. As the heights of the steps increase, the mixing efficiency increases. A higher mixing efficiency means that the jet is no longer concentrated in the core area of the jet, and has spread to a larger area, which is

consistent with that shown in Figures 14 and 15. With the effect of steps, the thickening of the shear layer in the windward area and the decrease of the mixture fraction gradient is the key to improving the mixing efficiency. Simultaneously, as the heights of steps increase, the CVP promotes mixing in leeward areas and increases the jet concentration near the wall. However, the step will bring more total pressure loss while improving the mixing performance. Figure 18b describes this phenomenon. The step reduces the total pressure recovery coefficient and advances the position of the total pressure attenuation.

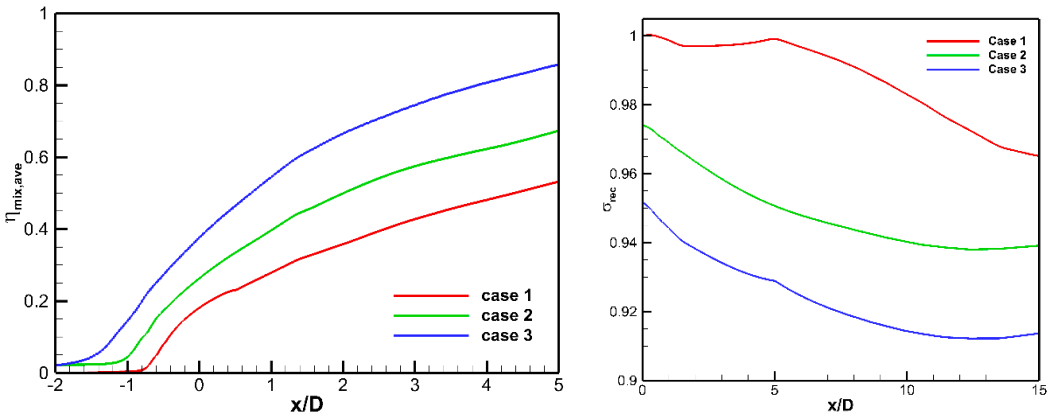

Figure 18. Time-averaged mixing efficiency (**a**) and total pressure recovery coefficient (**b**) along the flow direction for three cases.

5. Conclusions

In this paper, LESs of the transverse jet in supersonic crossflow in configurations with or without the BFS were carried out. The results prove that these cases have similar flow field structures and mixing mechanisms. However, with the influence of the large-scale recirculation zone formed by the steps, the distributions of velocity and pressure, the size of the separation zone, and the position and shape of the shock and shear vortex change. As a result, the local and overall mixing performance is different. By comparison and analysis of the results of different step height cases, this work reveals the effect of the BFS on the transverse jet and summarizes the influence of the step height in mixing performance.

1. Due to the large-scale subsonic recirculation zone induced by steps, the tilt angle of the barrel shock is reduced, and the bow shock is lifted from the wall. The change of the shock structure of the flow field is beneficial to the deepening of the jet penetration.
2. The shear layers on the windward region become thicker, and the shear effect of the large-scale structure is weakened. The convection velocity of the shear vortexes is reduced, resulting in more sufficient local mixing. The wake vortices are suppressed while the range of the CVPs expands, so that there is a deeper spread of the jet in the leeward zone.
3. The combined effect of the separation bubble and the upstream large-scale recirculation zone entrains the jet injectant into the upstream near-wall zone. The bow shock rising makes it easier for the vortex in the separation bubble to wind up the jet, and then it is entrained to the wall by the recirculation zone.
4. As the height of the step increases, the penetration of the jet in the near-field increases, and especially, an enhancement of its spread is more obvious. The mixing efficiency is significantly improved, which is positively correlated with the step height.

Author Contributions: Conceptualization: J.Z., Z.W., C.L. and J.Y.; Investigation: J.Z.; Methodology: M.S., H.W. and C.L.; Project administration: Z.W. and M.S.; Validation: J.Z.; Visualization: J.Z.; Writing—original draft: J.Z.; Writing—review and editing: J.Z., H.W., C.L. and J.Y. All authors have read and agreed to the published version of the manuscript.

Funding: This research received no external funding.

Conflicts of Interest: The authors declare no conflict of interest.

Nomenclature

D	injector diameter
D^{sgs}	turbulent energy dissipation term
E; **F**; **G**	inviscid fluxes
$\mathbf{E}_v$; $\mathbf{F}_v$; $\mathbf{G}_v$	viscid fluxes
J	jet-to-crossflow momentum flux ratio
Jp	penetration depth
Js	spread
k_{sgs}	subgrid turbulent kinetic energy
Ma	Mach number
P	static pressure
$P_k{}^{sgs}$	turbulent kinetic energy generation term
Pr_t	turbulent Prandtl number
Q	conservative variables
r_{st}	time-space correlation coefficient
T	static temperature
t	time
Δt	time interval
$\widetilde{u}_j$	velocity
x_j	spatial coordinates
Y''	fluctuation
Y''_{rms}	root mean square
ρ	density
Δ	filter width
τ_{ij}^{sgs}	sub-grid viscous stress tensor

References

1. Huang, W. Transverse jet in supersonic crossflows. *Aerosp. Sci. Technol.* **2016**, *50*, 183–195. [CrossRef]
2. Huang, W.; Du, Z.B.; Yan, L.; Xia, Z.X. Supersonic mixing in airbreathing propulsion systems for hypersonic flights. *Prog. Aerosp. Sci.* **2019**, *109*, 100545. [CrossRef]
3. Liu, C.; Wang, Z.; Wang, H.; Sun, M. Mixing characteristics of a transverse jet injection into supersonic crossflows through an expansion wall. *Acta Astronaut.* **2016**, *129*, 161–173. [CrossRef]
4. Gao, Z.; Lee, C. Numerical research on mixing characteristics of different injection schemes for supersonic transverse jet. *Sci. China Technol. Sci.* **2011**, *54*, 883–893. [CrossRef]
5. Lazar, E.; Elliott, G.; Glumac, N. Energy deposition applied to a transverse jet in a supersonic crossflow. *AIAA J.* **2010**, *48*, 1662–1672. [CrossRef]
6. Yang, H.; Li, F.; Sun, B. Trajectory analysis of fuel injection into supersonic cross flow based on schlieren method. *Chin. J. Aeronaut.* **2012**, *25*, 42–50. [CrossRef]
7. Huang, W.; Liu, J.; Jin, L.; Yan, L. Molecular weight and injector configuration effects on the transverse injection flow field properties in supersonic flows. *Aerosp. Sci. Technol.* **2014**, *32*, 94–102. [CrossRef]
8. Hariharan, V.; Velamati, R.K.; Prathap, C. Investigation on supersonic combustion of hydrogen with variation of combustor inlet conditions. *Int. J. Hydrogen Energy* **2016**, *41*, 5833–5841. [CrossRef]
9. Chang, J.; Zhang, J.; Bao, W.; Yu, D. Research progress on strut-equipped supersonic combustors for scramjet application. *Prog. Aerosp. Sci.* **2018**, *103*, 1–30. [CrossRef]
10. Choubey, G.; Pandey, K.M. Effect of different wall injection schemes on the flow-field of hydrogen fuelled strut-based scramjet combustor. *Acta Astronaut.* **2018**, *145*, 93–104. [CrossRef]
11. Abdel-Salam, T.M.; Tiwari, S.N.; Mohieldin, T.O. Effects of ramp side angle in supersonic mixing. *AIAA J.* **2003**, *41*, 1199–1201. [CrossRef]

12. Huang, W.; Li, S.-B.; Yan, L.; Wang, Z.-G. Performance evaluation and parametric analysis on cantilevered ramp injector in supersonic flows. *Acta Astronaut.* **2013**, *84*, 141–152. [CrossRef]
13. Pohlman, M.R.; Greendyke, R.B. Parametric analysis of pylon-aided fuel injection in scramjet engines. *J. Eng. Gas Turbines Power* **2013**, *135*, 024501. [CrossRef]
14. Vishwakarma, M.; Vaidyanathan, A. Experimental study of mixing enhancement using pylon in supersonic flow. *Acta Astronaut.* **2016**, *118*, 21–32. [CrossRef]
15. Barnes, F.W.; Tu, Q.; Segal, C. Fuel–air mixing experiments in a directly fueled supersonic cavity flameholder. *J. Propuls. Power* **2016**, *32*, 305–310. [CrossRef]
16. Park, G.; Park, C.; Jin, Y.; Choi, H.; Byun, J.; Hwang, K. Ethylene transverse jets in supersonic crossflows. *J. Propuls. Power* **2015**, *31*, 773–788. [CrossRef]
17. McDaniel, J.C.; Graves, J., Jr. Laser-induced-fluorescence visualization of transverse gaseous injection in a nonreacting supersonic combustor. *J. Propuls. Power* **1988**, *4*, 591–597. [CrossRef]
18. Karagozian, A.R.; Wang, K.C.; Le, A.T.; Smith, O.I. Transverse gas jet injection behind a rearward-facing step. *J. Propuls. Power* **1996**, *12*, 1129–1136. [CrossRef]
19. Mitani, T.; Ikeda, Y.; Nakajima, T.; Tomioka, S.; Kuratani, N. Mixing characteristics of normal injection into a supersonic backward-facing step flow measured with PIV. In Proceedings of the 40th AIAA Aerospace Sciences Meeting & Exhibit, Reno, NV, USA, 14–17 January 2002. [CrossRef]
20. Sharma, V.; Eswaran, V.; Chakraborty, D. Effect of location of a transverse sonic jet on shock augmented mixing in a SCRAMJET engine. *Aerosp. Sci. Technol.* **2020**, *96*, 105535. [CrossRef]
21. Sharma, V.; Eswaran, V.; Chakraborty, D. Determination of optimal spacing between transverse jets in a SCRAMJET engine. *Aerosp. Sci. Technol.* **2020**, *96*, 105520. [CrossRef]
22. Wu, J.; Wang, H.; Sun, M.; Zhang, S.; Wang, Z. Mixing Characteristics of transverse jet injection into supersonic flow after rearward-facing step. *Adv. Mech. Eng.* **2013**, *5*, 762595. [CrossRef]
23. Liu, H.; Wang, B.; Guo, Y.; Zhang, H.; Lin, W. Effects of inflow mach number and step height on supersonic flows over a backward-facing step. *Adv. Mech. Eng.* **2013**, *5*, 147916. [CrossRef]
24. Santiago, J.G.; Dutton, J.C. Velocity measurements of a jet injected into a supersonic crossflow. *J. Propuls. Power* **1997**, *13*, 264–273. [CrossRef]
25. Hassan, E.; Boles, J.; Aono, H.; Davis, D.; Shyy, W. Supersonic jet and crossflow interaction: Computational modeling. *Prog. Aerosp. Sci.* **2013**, *57*, 1–24. [CrossRef]
26. Liu, C.; Wang, Z.; Wang, H.; Sun, M.; Li, P. Large eddy simulation of cavity-stabilized hydrogen combustion in a diverging supersonic combustor. *Int. J. Hydrogen Energy* **2017**, *42*, 28918–28931. [CrossRef]
27. Toh, H.T. *Large Eddy Simulation of Supersonic Twin-Jet Impingement Using a Fifth-Order WENO Scheme*; Virginia Polytechnic Institute and State University: Blacksburg, VA, USA, 2004.
28. Yoshizawa, A.; Horiuti, K. A statistically-derived subgrid-scale kinetic energy model for the large-eddy simulation of turbulent flows. *J. Phys. Soc. Jpn.* **1985**, *54*, 2834–2839. [CrossRef]
29. Boles, J.; Choi, J.I.; Edwards, J.; Baurle, R. Multi-wall recycling/rescaling method for inflow turbulence generation. In Proceedings of the 48th AIAA Aerospace Sciences Meeting Including the New Horizons Forum and Aerospace Exposition, Orlando, FL, USA, 4–7 January 2010. [CrossRef]
30. Eberhardt, S.; Hickel, S. *Comparative Numerical Investigation of a Sonic Jet in a Supersonic Turbulent Crossflow*; Springer: Cham, Switzerland, 2015.
31. Kawai, S.; Lele, S.K. Large-eddy simulation of jet mixing in supersonic crossflows. *AIAA J.* **2010**, *48*, 2063–2083. [CrossRef]
32. Takahashi, H.; Masuya, G. Effects of injection and main flow conditions on supersonic turbulent mixing structure. *AIAA J.* **2010**, *48*, 1748–1756. [CrossRef]